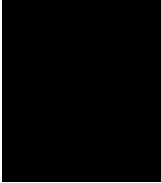
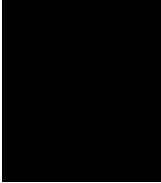
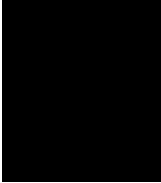
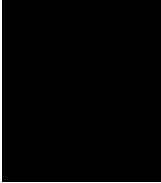
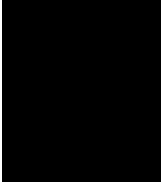


# The Effect of Orifice Configuration on Pintle Spray Cones

Final Report

Group #26

Sean Cornish (USCID:   
Zachary Fujita (USCID:   
Mark McDermott (USCID:   
Michael Smat (USCID:   
Patrick Trunfio (USCID: 

Presented to:

Dr. Robert Antypas, Dr. Akshay Potnuru, Dr. Charles Radovich, Dr. Yann Staelens

AME 441aL Senior Projects Laboratory

8 December 2021

## ABSTRACT

The configuration of orifices on a pintle injector for a bipropellant liquid rocket engine affects the direction and distribution of propellant flow in the mixed sheet that is produced by the collision of fuel and oxidizer flows. This mixed sheet is referred to as a spray cone. The angle at which the spray cone propagates into the chamber has been described for the visible upper surface of the spray with classical and empirical models based on the total momentum ratio ( $TMR$ ) of the colliding propellants for a single row of orifices, but the mass flow distribution within the spray has not been extensively researched. This study analyzes the effect of utilizing two rows of offset orifices separated by a gap  $H$  specified in multiples of orifice diameter  $D_o$ . The angle and mass flow distribution of the spray cone from pintle injectors with  $H/D_o$  ranging from 0 to 2.0 were evaluated with  $TMR$  ranging from 0.35 to 1.1 by collecting mass flow through intervals of spray cone angle. The results show similar mass flow distributions and trends with  $TMR$  for all  $H/D_o$  tested, demonstrating that multiple orifice rows may be considered as a design selection when the mass flow distribution as measured is accounted for. However, the angle measured to the upper surface of the spray cone did not agree with the angle of peak mass flow distribution at  $H/D_o \lesssim 1.0$ , indicating a circumferential deflection of the axial flow that bypasses the first row of orifices to increase impingement on the second row and increase the angle of peak mass flow. This demonstrates that existing spray cone angle research based on the trajectory of the upper spray cone surface may not properly identify flow momentum characteristics and lays the groundwork for the use of multiple orifice rows to increase mass flow in a given engine footprint.

# I. INTRODUCTION

## A. PINTLE INJECTORS

A pintle injector used on bipropellant liquid rocket engines features a single, central injection element that protrudes into the combustion chamber [1]. One propellant flows through this central element, known as the pintle, and is injected radially into the chamber by discrete orifices or a continuous slit. The other propellant is injected axially by an annulus concentric with the pintle circumference. The collision forms a combined flow that propagates into the chamber at an angle, as shown in Figure 1.

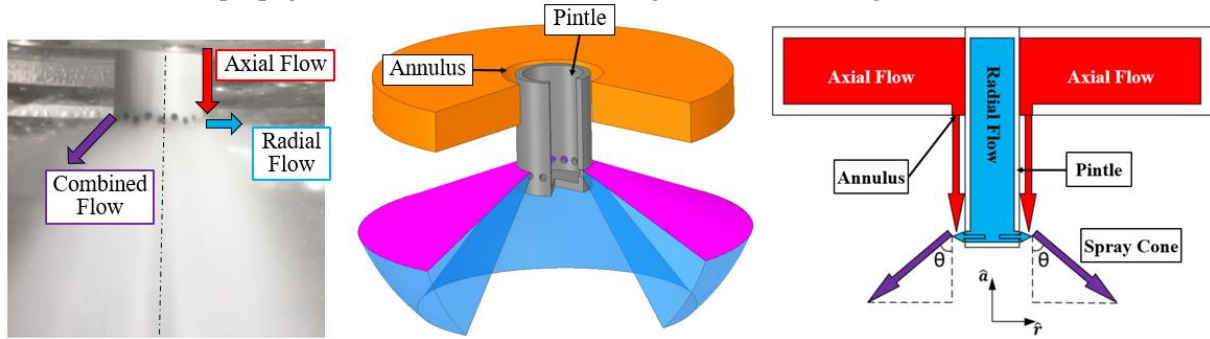


Figure 1. Illustration showing evolution of combined flow from axial and radial flow injected by the annulus and pintle elements, respectively.

Pintle injectors offer several advantages over other injector types. The central pintle element is simpler to manufacture than an impinging jet or swirl injector, while retaining the advantage of collision-driven mixing over showerhead injection. The use of a single, large element enables more throttling control in engines featuring a pintle with an annulus, as movement of a sleeve [2] or the pintle tip [3] can change the pintle outlet area. This enables immense throttling ratios compared to those feasible in a plate type injector [4]. Pintle engines also mitigate risk of combustion instability by distributing energy away from both the engine axis and the upper face of the chamber where pressure antinodes are located [5]. These characteristics have led to its use in multiple successful engine designs, including NASA's Lunar Descent Module Engine [6], SpaceX's highly reusable Merlin engine [7] [8], and university research teams [9].

Several geometric parameters of the pintle element affect spray behavior and must be optimized for an engine design. One of these is the configuration of the orifices on the pintle used to inject the radial flow. Although the injection behavior of pintles with radial orifices has been studied extensively [10] [11] [12], existing research has not studied the use of multiple rows of orifices, despite the potential advantages. Including multiple rows of orifices on a pintle would enable a greater mass flow rate for a given injector size. This would allow more thrust to be produced on a given engine footprint or enable a smaller pintle, which minimizes mass and cost from the expensive material required to withstand exposure to the flow environment in the combustion chamber.

Injection behavior in other flow regimes, particularly in fuel-air combustors, suggest geometric parameters that may govern how multiple rows of orifices affects pintle performance [13]. This study focuses on the effect of the distance between rows of orifices on the behavior of the combined flow, referred to as  $H$ . To provide a nondimensional description following the example of previous research [13],  $H$  is normalized by the primary geometric characteristic of the pintle orifices, the orifice diameter  $D_o$ , in a ratio  $H/D_o$ , illustrated in Figure 2.

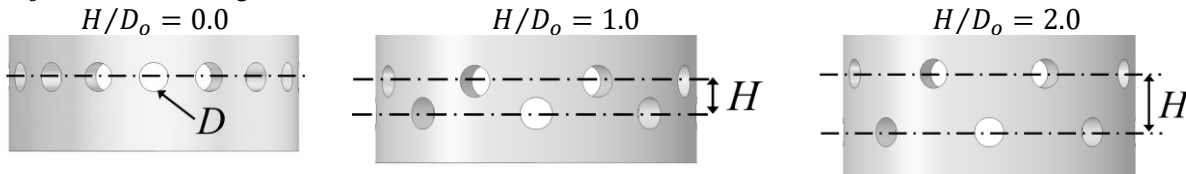


Figure 2. Illustration of the parameter  $H/D_o$  to change the configuration of pintle orifice rows.

As  $H$  is varied, another important geometric characteristic of pintle injectors changes: the axial distance between the annulus and the radial orifices,  $L$ . Normalized by the pintle diameter  $D_p$ , this parameter is known as skip distance ( $L_s$ ) and is defined as

$$L_s = L/D_p \quad (1)$$

$L_s$  has been shown to affect pressure wave formation, droplet size, and the angle of the combined flow, leading to an overall effect on combustion that maximizes efficiency at  $L_s \approx 1$  [3] [14]. To focus on the effect of  $H/D_o$  in this study, an effective skip distance  $L_{SE}$  was defined to describe the average skip distance to the two orifice rows, as shown in Figure 3.

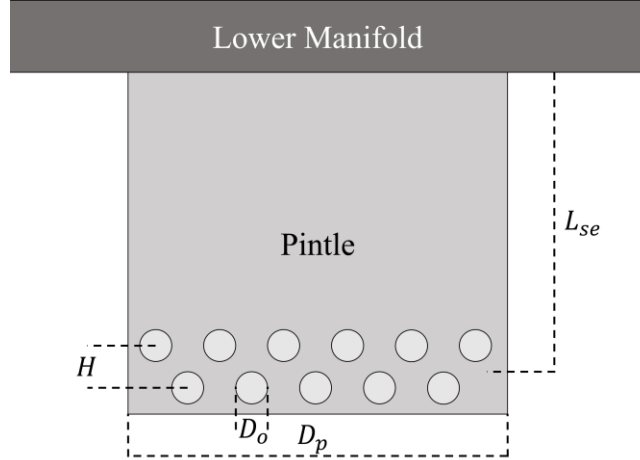


Figure 3. Effective skip distance of pintle injector with multiple rows of orifices

All  $H/D_o$  tested featured an effective skip distance of  $L_{SE} = 1$ , to isolate the unique effects of multiple orifice rows.

## B. INJECTOR CHARACTERISTICS

For pintle injectors, like other injector types, the orifice geometry required to achieve desired propellant momenta can be described by incompressible fluid flow relations. The thrust produced by a rocket engine is determined prior to an injector's design and is described by a total mass flow from the engine at a given chamber pressure [15]. Therefore, it is necessary to determine the upstream pressure that will achieve that mass flow through the injector. This relationship between mass flow rate  $\dot{m}$  or volume flow rate  $Q$  and feed pressure is described by

$$\dot{m} = C_d A \sqrt{2\rho\Delta P} \quad (2)$$

where  $A$  is the injector element area,  $\rho$  the propellant density,  $\Delta P$  the pressure drop across the element, and  $C_d$  the discharge coefficient of the injector element [15]. The discharge coefficient accounts for viscous swirling and boundary layer effects that reduce the velocity achieved across the injector area for a given pressure difference compared to an ideal inviscid injector. The average momentum of the injected flow is described by the average injection velocity achieved by the real injector. By substituting  $v = \dot{m}/\rho A$  for the average velocity across injection area  $A$ , the momentum of the injected flow becomes

$$\dot{m}v = \frac{\dot{m}^2}{\rho A} \quad (3)$$

allowing momentum to be calculated directly from the supplied propellant flow rate, density, and injector characteristics.

## C. SPRAY CONE ANGLE

Because it distributes flow and energy throughout the combustion chamber, the spray cone of a pintle injector must be characterized during the design process to optimize combustion efficiency [16], combustion stability [5], and thermal loads [17]. The spray cone must achieve sufficient propellant stay

time in the chamber to ensure complete combustion while avoiding impinging the flame front directly on the chamber walls, particularly in ablative chambers [2] [4]. Because of the difficulty modeling the complex multi-phase fluid dynamics that characterize the propellant collision at the pintle tip, spray cone behavior is estimated from empirical relations in literature before testing of an injector prototype. While testing of a specific design is ultimately a necessary validation step [4], starting with empirical relations from existing studies on similar geometries decreases the number of prototyped design iterations, saving time and money [8]. This emphasizes the need for research on pintles with multiple rows of orifices to characterize the effect of that parameter.

### 1. Momentum Ratios

Describing the spray cone from the momentum of the axial and radial flows is useful because the propellant mass flow rates and injector geometry allow momentum to be determined from incompressible fluid behavior as described above. A first-principles approach to the problem of the fluid collision predicts spray cone angle from the ratio of radial and axial momentums. This ratio, known as the total momentum ratio (*TMR*), is defined as

$$TMR = \frac{\dot{m}_r v_r}{\dot{m}_a v_a} = \left( \frac{\rho_a A_a}{\rho_r A_r} \right) \left( \frac{\dot{m}_r}{\dot{m}_a} \right)^2 \quad (4)$$

The first form of the expression illustrates the incorporation of the momentum rate of each fluid in the expression, while the second form substitutes for velocity as in (3).

The assumption of an inelastic collision between the axial and radial flows predicts a spray cone angle  $\theta$  from

$$\tan \theta = TMR \quad (5)$$

Geometry of the pintle, however, also has been observed to affect the relationship between  $\theta$  and *TMR*. For discrete pintle orifices, this effect is particularly pronounced. The discretization of the radial momentum creates a local momentum ratio (*LMR*) that varies around the pintle circumference: more radial momentum is introduced at the orifices, while more axial momentum is present at spaces between orifices. The local momentum ratio scales the annular momentum to consider only the portions of the flow colliding with radial flow, as defined by

$$LMR = \frac{\dot{m}_r v_r}{\left( \frac{Nd_o}{\pi d_p} \right) \dot{m}_a v_a} = \frac{TMR}{\left( \frac{Nd_o}{\pi d_p} \right)} \quad (6)$$

The scaling factor in the denominator is known as the blockage factor (*BF*):

$$BF = \frac{Nd_o}{\pi d_p} \quad (7)$$

The momentum ratios *TMR* and *LMR* nondimensionalize the fluid collision by describing the relative magnitude of the radial and axial momenta. This enables the use of water flow testing to evaluate the impact of geometric parameters since the density ratio of the flows is included in (4). Water flow testing is significantly less hazardous and expensive than testing with propellants, and through momentum ratios, can describe the dynamic behavior of the injector effectively.

Water flow research conducted previously has focused on momentum ratios as the primary parameter determining spray cone angle for a given injector geometry [2] [3]. These investigations have noted divergence from the analytical model shown in (5). While some models attempt to fit an empirical curve over a limited range of momentum ratios, the relationship between  $\theta$  and momentum ratio must satisfy the limits  $\theta \rightarrow 0$  as  $TMR \rightarrow 0$ , reflecting pure axial flow, and  $\theta \rightarrow 90^\circ$  as  $TMR \rightarrow \infty$ , reflecting pure radial flow. As shown in Table 1, several formulations have been proposed for liquid-liquid pintle injectors alone. The models most of interest in comparison to this work aside from the classical theory are those by Blakely et al. and Cheng et al. because these examine liquid-liquid pintle injectors with discrete orifices. The models by Escher and Lee are shown as examples of empirical fits intended to apply as approximations over a limited range of momentum ratios without satisfying the limits at  $TMR \rightarrow 0, \infty$ .

Table 1. Summary of proposed spray cone angle prediction models based on momentum ratios and additional parameters specified.

Author	Correlation for $\theta$	Additional Parameters	Flow Type	Radial Injection Type
Classical Theory	$\tan^{-1}(TMR)$	None	Not specified	Not specified
Blakely et al. [19]	$\alpha \tan^{-1}(\beta \cdot LMR) + C$	Related to Blockage Factor	Liquid-liquid	Discrete orifices
Cheng et al. [18]	$\cos^{-1}\left(\frac{1}{1+TMR}\right)$ OR $\cos^{-1}\left(\frac{1}{1+LMR}\right)$	None	Liquid-liquid	Both discrete orifices and annulus
Escher [11]	$(c_1 + c_2 TMR) \cdot TMR^{1/2}$	None	Liquid-liquid	Discrete orifices
Lee [3]	$c_1 + c_2 \cdot TMR \left(\frac{G}{L_S}\right)$	Skip Distance ( $L_S$ ) Orifice Height ( $G$ )	Gas-liquid	Annulus

A key distinction in output between these models and the classical inverse tangent relationship is the rate of change of spray cone angle as  $TMR$  increases. This quantity, the derivative  $d\theta/d(TMR)$ , will be expressed for simplicity as  $\lambda$  with the definition

$$\lambda \equiv \frac{d\theta}{d(TMR)} \quad (8)$$

$\lambda$  can be used to describe overall trends in  $\theta$  over a range of momentum ratios. Nonlinear empirical models such as those proposed by Cheng, Escher, and Blakely predict a greater  $\lambda$  at low  $TMR$ , with a sharper leveling off to satisfy the asymptotic condition of  $\theta = 90^\circ$  as  $TMR \rightarrow \infty$ .

## 2. Mass Flow Distribution

While  $LMR$  seeks to account for momentum distribution at the orifices, it does not assess the annular flow that continues past the orifices, known as bypass flow. Because of bypass flow, the distribution of flow within the spray cone may not be entirely uniform. Lee et al. employed structured laser illumination planar imaging (SLIPI) to assess spray uniformity in their experiments, but only to show that flow was distributed evenly through the spray cone for a single test run for a single row of orifices rather than how the distribution changes under different flow conditions [3]. Most other research assesses spray cone with an optical measurement of the upper surface of the spray cone [3] [14] [18] [19] [20]. As demonstrated in Figure 4, this upper surface may conceal the actual mass flow distribution at a lower spray cone angle.

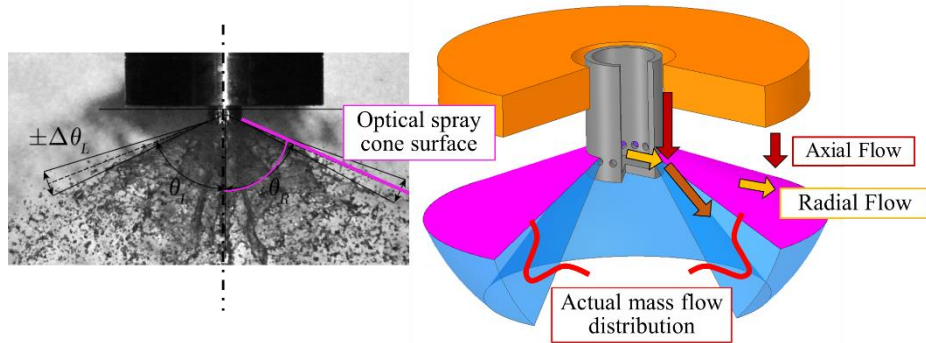


Figure 4. Comparison of spray cone measurement in previous work based on the visible upper extent of flow [10] to possible mass flow distribution within the spray cone.

This is of particular concern in considering the impact of multiple rows of orifices: by distributing the introduction of radial momentum over a greater distance, the distribution of the injected mass flow may be affected. Moreover, the effect of the collision at the first row of orifices on the behavior at the second

row is uncertain. The effect of *TMR* or *LMR* on the spray cone from a pintle with multiple orifice rows might be hypothesized for different cases in Table 2.

Table 2. Possible descriptions of the effect of rows of orifices on mass flow distribution and spray cone angle.

Defining Parameter	Reduction of Bypass Flow Momentum	Change in <i>TMR</i> of Orifice Row	Hypothetical Effect on Spray Cone
<i>TMR</i>	Small	-	The first row of orifices has comparatively lower radial momentum relative to the full axial flow, reducing $\theta$ . At the second row, even with negligible effect on the bypass flow, the reduced axial flow leaves a higher momentum ratio. A different $\theta$ propagating from offset holes would likely produce a more diffuse spray cone.
		+	
	Large	-	Momentum ratio at the second row would be greater, exaggerating the effects postulated for a small effect on bypass flow.
		+	
<i>LMR</i>	Small	=	The relationship between axial and radial momentums is unchanged at both collision points, resulting in the same spray cone angle from multiple rows of orifices as from a single row.
		=	
	Large	=	The second row of orifices is subject to significantly different axial momentum, potentially altering spray cone behavior.
		+	

Because optical spray cone angle measurements capture only the upper surface of the spray cone, the optical spray cone measurement is more significantly affected by changes in radial momentum than the mass flow distribution, which still incorporates the bypass flow. To distinguish spray cone angle measurements,  $\theta_v$  will be used to denote the optical (“visual”) spray cone angle, while  $\theta_m$  will represent the spray cone angle of the mass flow distribution.

## II. EXPERIMENTAL DESIGN

To collect the necessary data, a modifiable pintle injector, feed system, and mass collection apparatus were procured. These components were designed, manufactured, and assembled into the configuration as shown in Figure 5.

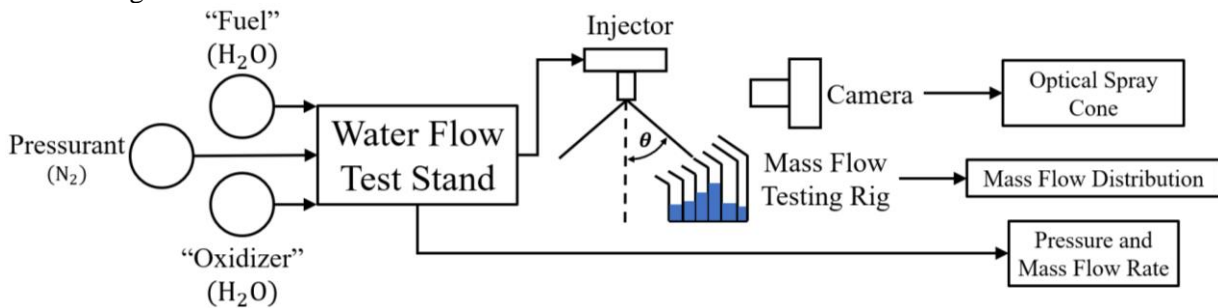


Figure 5: System level overview of complete experiment and data collection methods.

As shown, a water flow test stand was used to control flow of fuel and oxidizer (simulated with water) using  $N_2$  as a pressurant. The flow was driven through pintle injectors of varying  $H/D_o$  ratios. Data was collected through three collection methods: the optical spray cone angle  $\theta_v$  measured by an external camera, the mass spray cone angle  $\theta_m$  determined by the mass flow testing rig, and flow characteristic data collected through the water flow test stand.



## A. TEST ARTICLE

The injector to be used in this study was sized for a 1200 lbf liquid oxygen/kerosene engine. Complete high-level design parameters and the design procedure described in Appendix E produced the design point flow characteristics and pintle geometry listed in Table 3. A cross-section view of the injector with these parameters is shown in Figure 6(a).

To reduce cost and manufacturing lead time for this experiment, a prototype was produced from aluminum 6061, shown disassembled in Figure 6(b).

Table 3. Design point characteristics selected to meet the requirements in Appendix E. Additional outputs used in component sizing are provided in Appendix A.

Fuel Mass Flow Rate [kg/s]	0.653
Oxidizer Mass Flow Rate [kg/s]	1.415
Mixture Ratio	2.20
Pintle Diameter [mm]	18.8
Number of Pintle Orifices	20
Orifice Diameter [mm]	1.59
Annulus Width [mm]	0.32
Blockage Factor	0.54

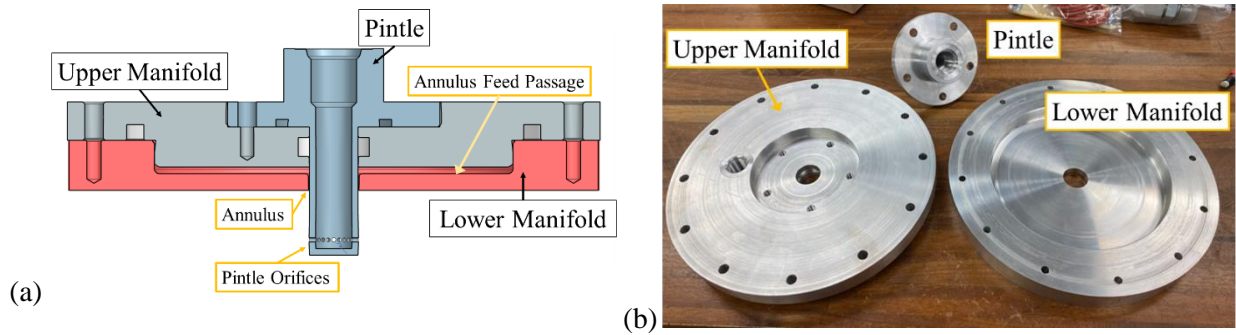


Figure 6. Illustration of the pintle used as a test article, with (a) a cross-sectional view of injector CAD and (b) the disassembled aluminum 6061 prototype.

## B. WATER FLOW TEST STAND

### 1. USC Liquid Propulsion Lab Water Flow Test Stand

The feed system used for conducting experiments and collecting data was the USC Liquid Propulsion Laboratory's Water Flow Test Stand (WFTS). The stand, seen in Figure 7, supports two 30L water tanks with feed pressures that can be varied between 200 and 6800 kPa. A regulated nitrogen bottle pressurizes the system and all pneumatic valves. The WFTS P&ID is provided in Appendix D.

### 2. EPR Tuning and Pressure Fluctuations

The test article pressure at both the pintle and annulus were controlled by adjusting the pressure setpoint of two TESCO ER5100 model electronic pressure regulators (EPRs) upstream of the water tanks. Both EPRs used proportional-integral-derivative (PID) controllers to bring each tank to their setpoint pressures and correct for any pressure deviations from the setpoints during flow where tank pressure drops would constantly drop. Through an iterative process, the EPRs were tuned such that tank pressures throughout each test would fluctuate around the setpoint rather than continuously decrease.

### 3. Instrumentation

The DAQ unit is an integrated system custom built using NI chassis with NI modules for each sensor. For the experiments run, the instrumentation included four Omega LCCA-50 S-load cells and eight Omega PX319 series pressure transducers ranging from 200 psi to 5000 psi max pressure. A tabulated list of the key sensors used for data collection is given in Appendix E. The four load cells beneath the water collector



Figure 7. LPL WFTS CAD [21]

box provide the mass of water collected in the basin over time, providing an average mass flow rate as described in Appendix A. The critical pressure transducers for this experiment were mounted via stainless steel sense lines at the test article, on both the annulus and pintle lines, as well as at the water tanks. Both force and pressure data were collected at a sampling rate of approximately 800 Hz.

### C. MASS COLLECTION BASIN

The mass flow distribution of the spray cone was measured with a custom mass flow collection rig was designed and manufactured. The apparatus separated flow in  $5^\circ$  increments of  $\theta$  in one tenth of a rotation about the pintle axis (a  $36^\circ$  azimuthal angle). The measurable spray cone angle ranged from  $5^\circ$  to  $85^\circ$  to capture diffuse mass flow distribution at the outer ranges of  $TMR$ .  $5^\circ$  was chosen as the minimum angle that could be practically assembled with the accessible precision and raw material available. With 20 pintle holes, one tenth of a rotation includes two orifices, ensuring that for pintle configurations with  $H/D_o \neq 0$ , flow from both rows of orifices would be collected. To accomplish this, the collection area decreases at smaller spray cone angles (intervals more directly underneath the pintle) because of the nature of the spray propagation from the pintle. For the apparatus to measure one tenth of the flow, the open area of the measured sector rotates along a curved surface shown in Figure 8.

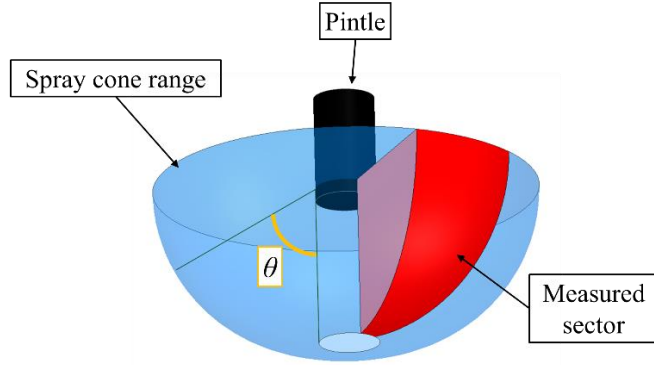


Figure 8. Illustration of the spray measurement area from the spherical propagation of spray from the collision location.

The finalized mass flow collection apparatus design as manufactured is shown in Figure 9. The acrylic components were laser cut, while a water jet cutter was used to shape each aluminum divider. The complete test apparatus was structurally supported by a stand manufactured from aluminum T-slot extrusions.

The aluminum dividers shown in Figure 9 divided the spray cone in increments of  $5^\circ$ . At the back of each divider, a vinyl tube was affixed to guide the flow to one of the six mass collection bins below during a test. For each test run, several steps were taken to collect mass flow data. Using (5), the expected spray cone angle for a given test  $TMR$  was predicted. The six increments in  $\theta$  on the testing apparatus closest to the predicted spray cone angle were selected to collect mass from the spray cone. The vinyl tube for each of the increments would then be guided to a different collection bin. After a test was finished, the collection bins were removed and massed before being dried and replaced for subsequent tests.

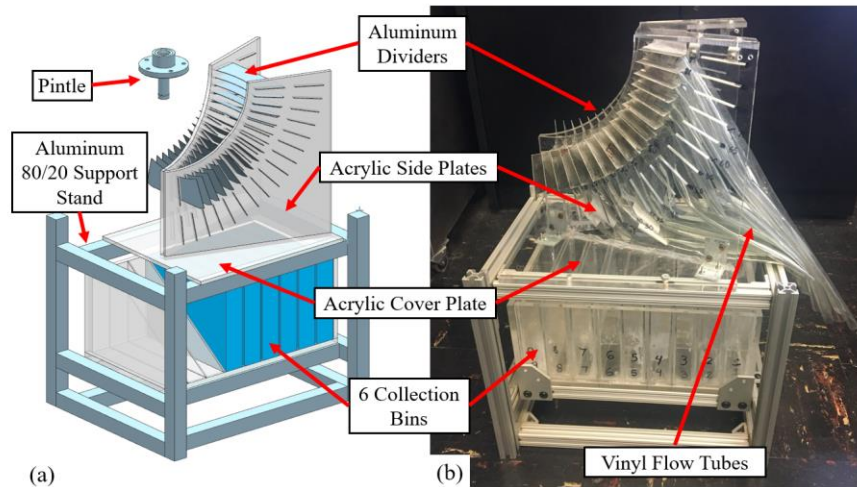


Figure 9: Mass flow distribution data collection rig. (a) shows the modelled design. (b) shows the assembled device as used for testing.



#### D. TESTING PARAMETERS

Five pintles were manufactured, each with a different row spacing. The parameter  $H/D_o$  varied from 0 to 2.0. Because alterations to the bypass flow from the first row of orifices are not known,  $TMR$  was used to set the parameter range for tests. As shown in (6) and (7), linear relationships can be transformed between  $TMR$  and  $LMR$  using  $BF$ . Namely, for  $\lambda$ , substitution using the definitions in (6) and (7) shows

$$\lambda_{LMR} = \lambda_{TMR} \cdot BF \quad (9)$$

Based on the supply pressures available from the LPL WFTS,  $TMR$  varied from approximately 0.4 to 1.1. At least five tests were conducted for each pindle  $H/D$  across this  $TMR$  range. With the fluctuations in pressure described above, the  $TMR$  could not be set precisely beforehand but could be determined for a test from the pressure transducer data.

Testing occurred in two stages. First, the discharge coefficients for the annulus and the pindle, provided in Table 4, were determined from single-flow tests described in Appendix B.

The second stage conducted combined flow tests, with simultaneous flow through both the pindle and the annulus. The discharge coefficients were used to calculate the mass flow rate through the injector based on the pressure drop from a transducer immediately upstream of the injection element based on (2).

Table 4. Discharge coefficients measured from single-flow tests for the pindle and annulus.

	$C_d$	$\Delta C_d / C_d$
Pindle	0.60	4%
Annulus	0.57	3%

#### E. OPTICAL SPRAY CONE MEASUREMENT

To analyze spray cone angle optically, video was taken inside the acrylic collection basin, with a camera centered on the pindle, at the height of the orifices and facing perpendicular to the direction of annular flow. Each video was named and saved according to its  $TMR$  and  $H/D_o$  configuration. For each video, 2 screenshots were taken several seconds apart in the test, giving two images per test case to optically analyze. Each image was imported to an optical analysis software where an angle was traced along the left and right edge of the spray cone at both the upper and lower boundary of where the spray cone angle could be reasonably argued to lie, as seen in Figure 10. This parameter is loosely defined in prior literature but is generally understood to be somewhere between the flow path of large droplets and the boundary of gradually finer mist [19]. For this study, optical spray cone was defined as the mean angle between the upper and lower reasonable boundary across 4 different cases per orifice row configuration: the left and right sides of two separate images. Uncertainty for these measurements was defined as maximum difference between an upper and lower boundary across the 4 cases added to the maximum disagreement between a left and right side of a single image [19].

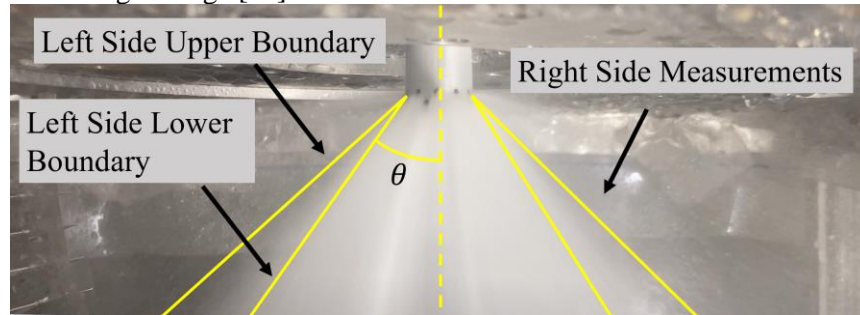


Figure 10. Sample image of optical spray cone measurements.

### III. RESULTS

#### A. TESTING SUMMARY

Each pindle was tested at least five times, collecting mass flow distribution and optical spray cone angle data at the five targeted  $TMR$ s. Table 5 shows the targeted pressure drops across both elements of the test article to achieve the corresponding  $TMR$  calculated using the experimentally derived discharge

coefficients. These pressure drops varied due to the differences in outer diameter of the pintles, and therefore flow area of the annulus.

Table 5: Element pressure drops for each pindle at each TMR

			<b>Pintle H/D</b>				
			0.0	0.5	1.0	1.5	2.0
			<b>Element Pressure Drop [psi]</b>				
<b>TMR</b>	0.35	Pintle	19	20	19	19	20
		Annulus	130				
	0.47	Pintle	27	28	26	24	27
		Annulus	130				
	0.60	Pintle	33	34	32	31	34
		Annulus	130				
	0.80	Pintle	44	45	43	42	45
		Annulus	130				
	1.10	Pintle	61	62	61	57	63
		Annulus	130				

The quantities required for each test are shown in Table 6. Once all inputs and testing inputs were provided, the test matrix generated plots containing data for the mass flow distribution within the spray cone at the angular span covered by the bins.

Table 6: Information required and produced by the test matrices

<b>Subsystem</b>	<b>Inputs</b>	<b>Intermediate Calculations</b>	<b>Testing Inputs</b>	<b>Testing Outputs</b>
Annulus	Diameter	Flow Area	Tank Pressure	Pressure trace
	Discharge Coefficient			
Pintle	Orifice Diameter	Flow Area	Tank Pressure	Pressure trace
	Number of Holes			
	Outer Diameter			
	Discharge Coefficient			
Collection Bins	Dry mass of all	-	Angular Span	Wet mass of all
Flow	Water Density	-	-	-
	Test duration			

Due to the maximum continuous angular span of collected water being 30°, the placement of the water collection bins was calculated and adjusted between tests when needed. This caused the peaks of the mass distributions to vary in location between tests, occasionally falling outside of the angular span covered by the bins. This effect can be seen in the qualitative representation of the plots generated for each pindle at each TMR in Table 7. In these plots, the vertical axis represents the mass of water collected, and the horizontal axis represents the angular span of the bins. Table 7 shows qualitatively that for each test there was an absolute or global maximum value at the bin which collected the most water.

The data from single tests representative of overall patterns are shown in Figure 11. As previously mentioned, due to the nature of the test setup and feasible angular resolution, each data point represents a 5-degree angle range plotted at the mean angle. A “Gaussian”-like spread is shown in Figure 11(a) which reveals the point at which the most mass was collected is at an angular range lower than the maximum angle range in which water was collected. It should also be noted that during several tests, especially at a TMR of 1.1, there exist two local maxima. These double peaks are a manifestation of a “double spray cone,” or a test in which there were two 5-degree angular ranges, which were separated by at least one additional 5-degree range, where the bulk of the spray cone mass was distributed. An example of this double spray cone can be seen in Figure 11(b).

Table 7: Qualitative representation of mass flow distribution data collected by catch basin for each pintle at each TMR

		<b>H/D</b>				
		0.0	0.5	1.0	1.5	2.0
<b>TMR</b>	0.35					
	0.47					
	0.60					
	0.80					
	1.10					

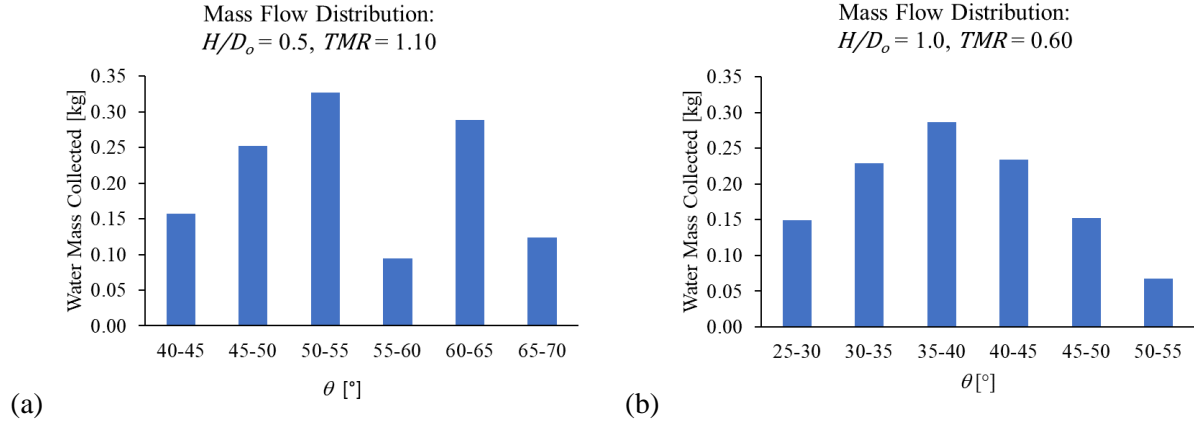


Figure 11. Single test data sets from (a)  $H/D_o = 1.0, TMR = 0.60$  and (b)  $H/D_o = 0.5, TMR = 1.10$

## B. DATA ANALYSIS

The distributions shown in the test runs above indicate that  $\theta$  can be assessed for a test run through two observations: the location of the peak collected mass and the location of the centroid of mass collected in all six bins. Because of challenges in precisely predicting and aligning the 30-degree spray cone measurement window of the mass flow distribution apparatus with the spray cone observed during a test run, the peak mass flow collected was not always centered in the bin distribution. However, a test was repeated until a peak was captured within the measurement window with at least one bin with a lower collected mass on each side of the peak bin.

The peak mass flow is indicated by a larger dot in a vertical series on the charts in Figure 12. Noting the linear trend in the location of the peak mass flow with respect to  $TMR$ , a linear best fit line was also generated to compare the effect of  $H/D$  and the trend in the optical spray cone. The data for each  $H/D_o$  in Figure 12 show a linear trend in the angle of peak mass flow with respect to  $TMR$  that falls underneath  $\theta_m$  at low  $TMR$  but converges at the upper range examined where  $TMR \approx 1.1$ .

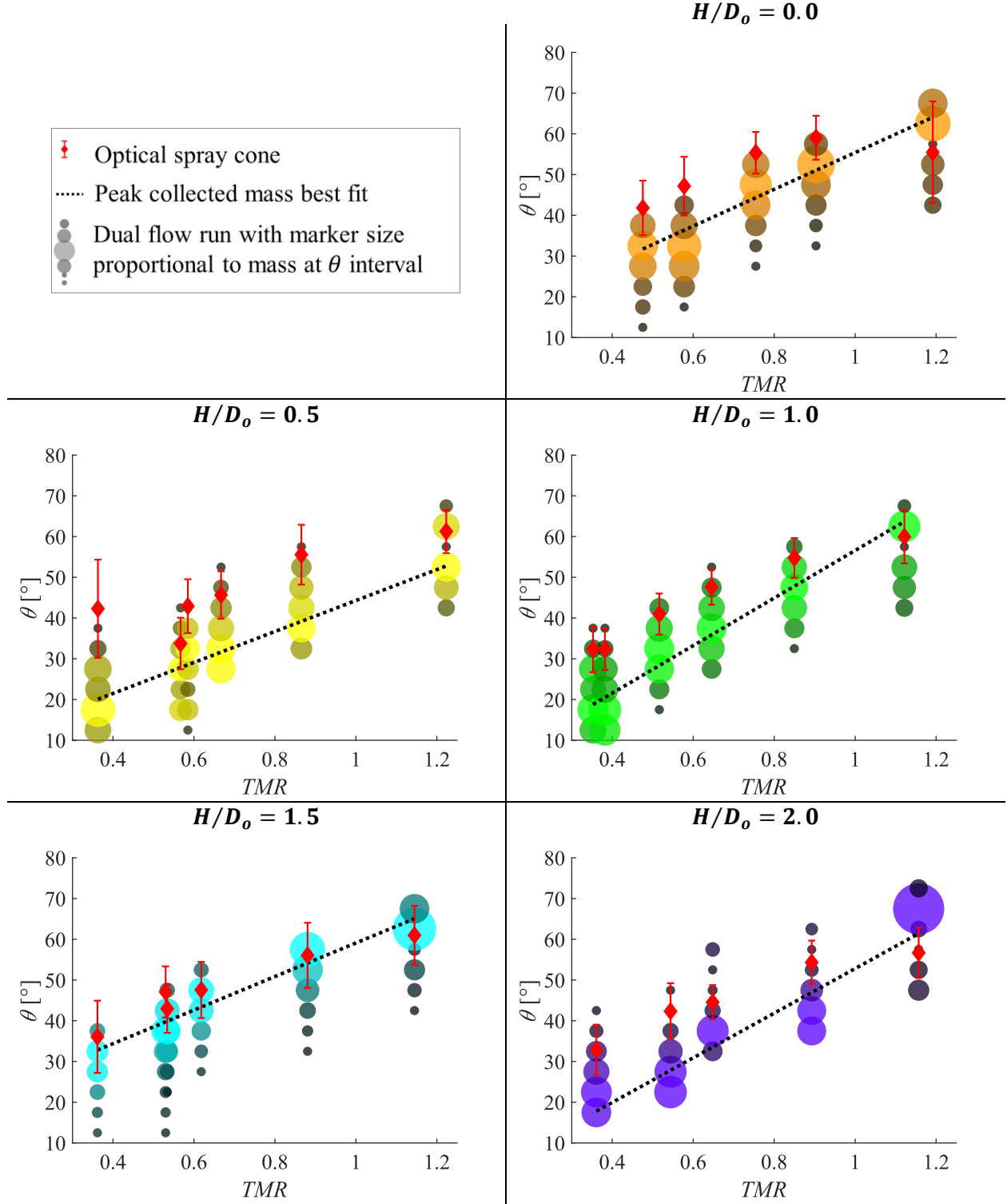


Figure 12. Summary of dual flow test data collected showing mass collected at different angular stations by the mass flow distribution apparatus. As indicated in the legend, a single test run, conducted at a single value of  $TMR$ , is recorded as a vertical series of dots with size proportional to recorded mass. The black dashed line corresponds to a linear regression best fit of the spray cone angle of the peak mass flow collected for a test run.

Although a linear trend does not respect the limiting behavior as  $TMR \rightarrow 0$  or  $TMR \rightarrow \infty$ , the slope  $\lambda$  obtained from  $\theta_m$  and  $\theta_v$  illustrates key effects over the range of momentum ratios considered. Moreover,

as referenced in Table 1, linear fits have been used previously to describe trends in spray cone angle.  $\lambda$  from  $\theta_m$  and  $\theta_v$  given in Table 8 show  $\theta_m$  increasing more rapidly with  $TMR$  than  $\theta_v$ , which remains oriented more in the radial direction than  $\theta_m$ , as the angles move towards convergence at the upper bound of  $TMR$ .

Table 8. Best-fit line calculation performed on peak and optical spray cone angle measurements. As described previously, the  $\lambda$  developed based on  $TMR$  may be scaled to a trendline with respect to  $LMR$  by dividing by the blockage factor:  $\lambda_{LMR} = \lambda_{TMR} \cdot BF$ .

$H/D$	$\theta_m = \lambda \cdot TMR + b$			$\theta_v = \lambda \cdot TMR + b$		
	$\lambda$ [°]	$b$ [°]	$R^2$	$\lambda$	$b$	$R^2$
0.0	45.13	10.3	0.956	19.72	36.4	0.621
0.5	38.02	6.3	0.961	28.57	26.6	0.739
1.0	58.39	-1.8	0.979	37.85	20.3	0.954
1.5	41.19	17.9	0.938	30.51	27.8	0.939
2.0	54.77	-2.0	0.857	29.99	24.5	0.934

Although the entirety of the spray flow was not collected in six bins, considering the centroid of the mass collected under the assumption that the angle range containing the peak contains the majority of the mass flow shows much lower variation in  $\lambda$  with respect to  $H/D$ , as presented in Table 9. The low variation in  $\lambda$  with respect to  $H/D$  indicates that, to the precision possible with this test apparatus, varying  $H/D_o$  appears to have minimal effect on the parameters driving the relationship between  $\theta$  and  $TMR$ . Comparison of  $\theta_m$  and  $\theta_v$  directly shows that  $\theta_v \geq \theta_m$  for all tests.  $\theta_v$  is also noted to closely match  $\theta = \tan^{-1}(LMR)$ , as indicated in Figure 15.

Table 9. Parameters of the best fit line determined from the centroid of the collected mass flow.

$H/D$	$\theta_m = \lambda \cdot TMR + b$		
	$\lambda$ [°]	$b$ [°]	$R^2$
0.0	42.96	8.5	0.971
0.5	40.00	6.6	0.963
1.0	45.01	6.7	0.973
1.5	44.45	10.3	0.938
2.0	46.80	8.1	0.949

### C. QUALITATIVE OBSERVATIONS

Two qualitative phenomena were observed that stood out in comparison to results from previous studies. The first of these was penetration of the annular sheet by the radial jets from each orifice. In Figure 13, an example of this irregularity is visible. On the right-hand side of the spray cone, the flow from a single orifice is noticeably higher and inconsistent with the rest of the spray cone. This breakthrough was more prominent and consistent at higher  $TMR$  tests.

The spray cone in the present work featured a pronounced difference in appearance compared to existing literature. In our tests, the spray cone atomized almost immediately, markedly different than previous studies that showed sheet breakup into large droplets. This contrast is presented in Figure 14.

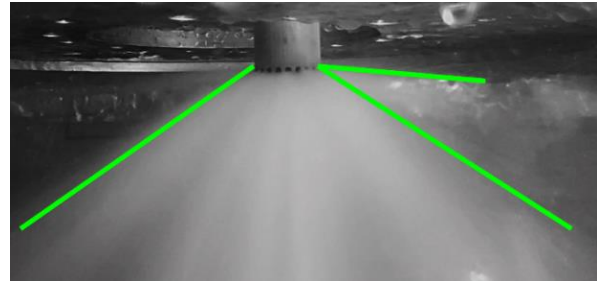


Figure 13: Representative image of radial penetration showing lines used for measurement of  $\theta_v$  where the radial penetration alters the optical angle.

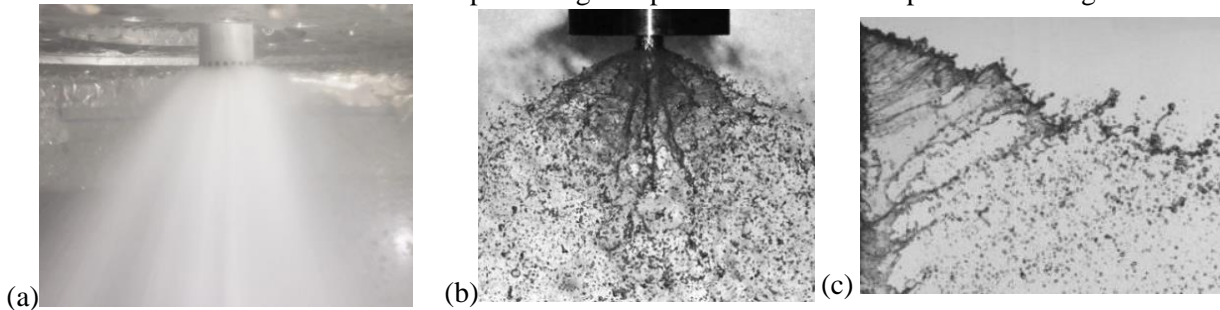


Figure 14. Comparison of pintle spray cones examined in (a) the present work and adapted results from previous work: (b) Blakely et al. [10] and (c) Cheng et al. [18].

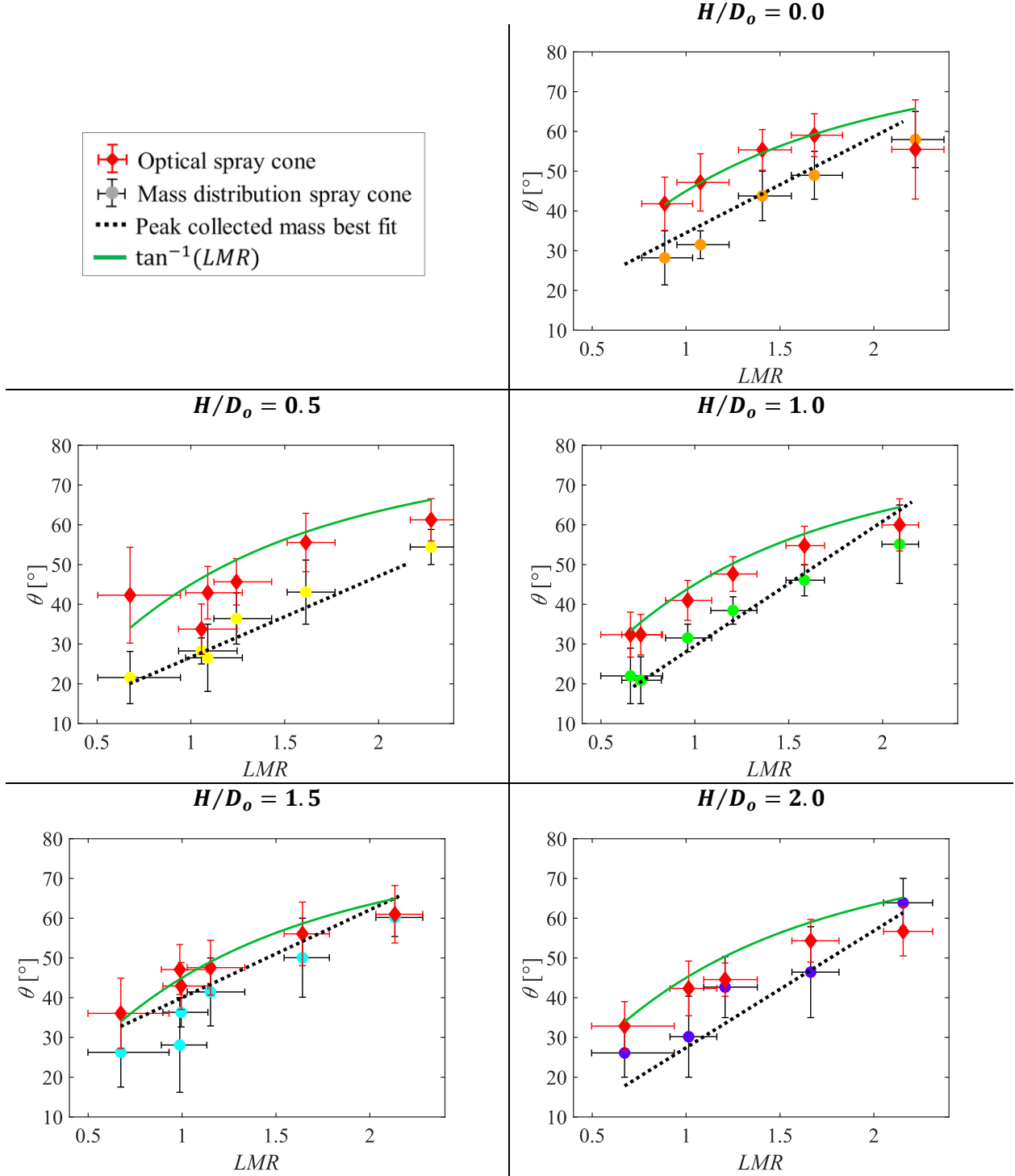


Figure 15. Detailed comparison of  $\theta_v$  and  $\theta_m$  to illustrate the consistent measurement of a greater spray cone angle by optical means compared to that realized with the mass flow distribution.

The increased atomization in the present work likely results from the high pressure drop suited for the engine that was the design basis for this test article according to the parameters in Table 3 and Appendix C. Atomization effects are beyond the scope of this study; however, because the spray still moves linearly, as shown in Figure 13 and Figure 14, the description of a spray cone and its measurement with the mass distribution apparatus still apply.



#### IV. DISCUSSION

The overall trends of spray cone angle and mass flow distribution with momentum ratio for each  $H/D_o$  shown in Figure 12 illustrate that introducing multiple rows of orifices does not substantially alter the mass flow distribution within the spray cone itself that would support concerns of poorer mixing performance. Rather, changes to spray cone behavior introduced with  $H/D_o$  of two rows of orifices are shown from both a direct comparison of  $\theta_v$  with  $\theta_m$  and the derived parameter  $\lambda_v$  and  $\lambda_m$ .

$\theta_v$  closely matches the function  $\tan^{-1}(LMR)$  for all  $H/D_o$ , but exceeds  $\theta_m$  considering uncertainties, only up to  $H/D_o = 1.0$ , as shown in Figure 15. At higher  $H/D_o$ ,  $\theta_v$  and  $\theta_m$  cannot be distinguished. This indicates that while the inverse tangent from classical theory may describe the initial collision at the upper row of orifices, and thus match  $\theta_v$ , this approach does not describe the trajectory of mass flow from the pintle for  $H/D_o \gtrsim 1.0$ . The close match between  $\theta_v$  and  $\tan^{-1}(LMR)$  for all  $H/D_o$  suggests, per Table 2, that  $LMR$  is the dominant parameter describing momentum behavior at the upper surface of the spray cone, since it remains constant at each orifice row. The convergence of  $\theta_v$  and  $\theta_m$  as  $H/D_o$  increases suggests that the  $LMR$  at the second row of orifices increases, effectively increasing  $\theta_m$ . Following the reasoning of Table 2, as  $H/D_o$  increases past 1.0, the effect of the first row of orifices on the bypass flow reduces the axial momentum carried through the second row of orifices, leading to an increase in  $\theta_m$  while  $\theta_v$ , determined from the  $LMR$  at the first row of orifices that forms the upper surface of the spray cone, remains unaffected. Following a hypothesis about the effect of orifices on the bypass flow proposed in [19], a deflection of the bypass flow introduced by the first row of orifices may reduce the amount of axial flow that can proceed unimpeded through the collision region and lower  $\theta_m$ . Figure 16 demonstrates how a deflection  $\gamma$  from the first row of orifices still permits some bypass flow at low  $H/D_o$ . As  $H/D_o$  increases, deflected axial flow may increasingly impinge on orifices of lower rows.

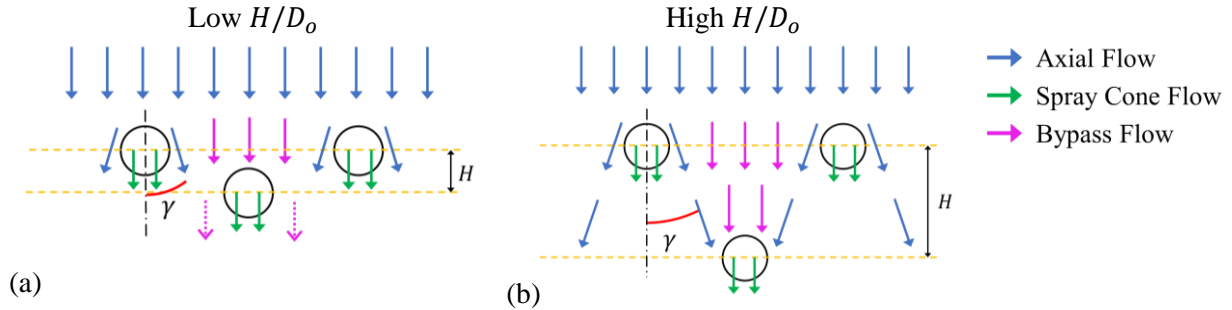


Figure 16. Illustration of flow deflection  $\gamma$  from the first row of orifices for (a) low  $H/D_o$ , indicating flow that bypasses both rows of orifices, compared to (b) high  $H/D_o$ , where  $\gamma$  is sufficiently high to impinge all bypass flow from the first row on second-row orifices.

Notably, although the  $LMR$  at the collision point itself may decrease at higher  $H/D_o$  because more axial flow impinges on the radial jet, the partial or complete elimination of flow that bypasses both orifice rows may increase  $\theta_m$  overall. For design purposes, this may be more desirable to ensure all propellant injected mixes, rather than continuing in the axial direction directly out of the nozzle.

The behavior of  $LMR$  as the defining parameter of the collision between the axial and radial flows is reflected in the consistency of  $\lambda_v$  and  $\lambda_m$  with  $H/D_o$  shown in Table 8 and Table 9. A different governing parameter, or a functional relationship different than the inverse tangent, at the second row of orifices would produce a different rate of change of  $\theta$  with momentum ratio. Rather, the consistency of  $\lambda$  with  $H/D_o$  indicates that the effect of bypass flow is an offset of the mass flow distribution, a conclusion that aligns with the hypothesis that the source of change in  $\theta_m$  is the amount of axial flow that bypasses both orifice rows.

$\lambda$  further illustrates the role of the bypass flow through a direct comparison  $\lambda_v$  and  $\lambda_m$  at  $H/D_o = 0$  with models developed on a single row of orifices. Figure 17 demonstrates the shallower slope of existing empirical fits for spray cone angle that align more closely with the optical spray cone angle measured for this study, while the steeper linear trend from mass flow collection is closer to the classical relation.

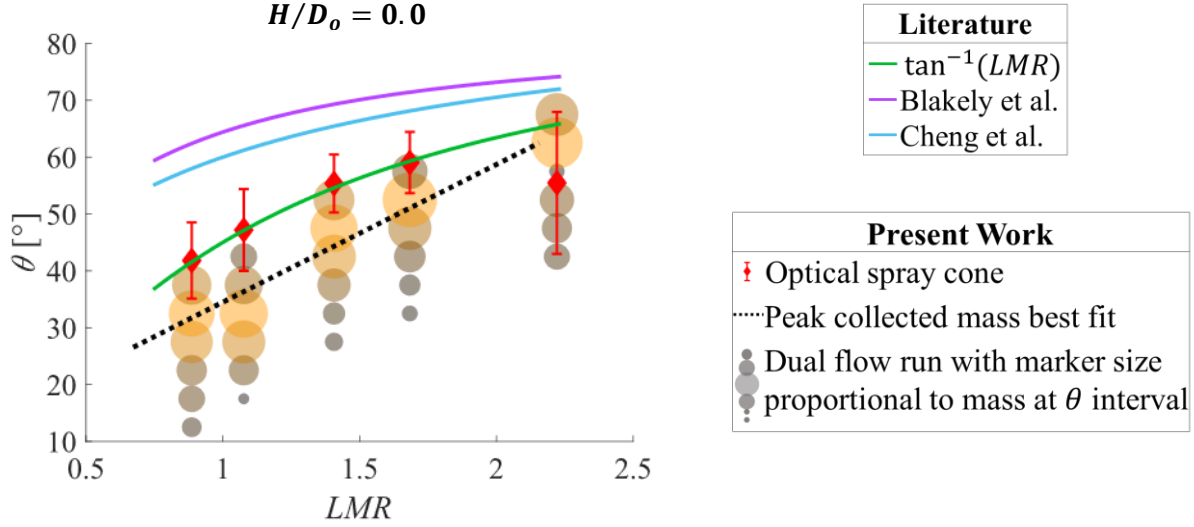


Figure 17. Comparison of mass flow distribution, optical spray cone angle, and predictions from literature for spray cone angle as a function of local momentum ratio ( $LMR$ ).

$\lambda_v < \lambda_m$  over this range of momentum ratios is reflective of a steeper increase in  $\theta$  at low  $TMR$  to satisfy the limit  $\theta \rightarrow 0^\circ$  as  $TMR \rightarrow 0$ . In the model proposed by Blakely et al. [19], a y-intercept offset is proposed to account for the minimum spray cone angle of  $20^\circ$  the researchers were able to achieve, even at  $TMR$  near 0. The behavior of these models at low  $TMR$  compared to data collected in the present work is shown in Figure 18. This clearly indicates an optical spray cone angle is not indicative of the mass flow distribution, as at momentum ratios near 0 almost all mass flow is in the axial direction. Similarly, in the present work, the linear fit based on optical spray cone angle exhibits a y-intercept  $b$  of greater than  $20^\circ$  at all  $H/D_o$  to accommodate the reduction in  $\lambda$ . In comparison, the linear fits of mass flow peak and centroid in Table 8 and Table 9 give a lower  $b$  than  $20^\circ$  in a range including  $0^\circ$ , reflecting how mass flow rate is more representative of the momentum characteristics of the spray cone than the angle of the upper surface.

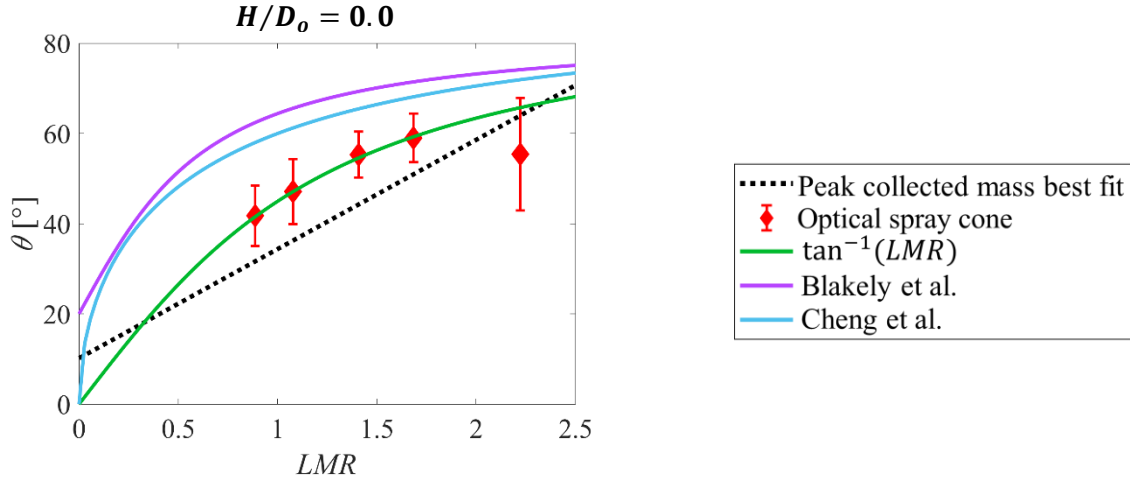


Figure 18. Comparison of model behavior including the limit at  $LMR = 0$  to illustrate the steeper increase at low  $LMR$  of models based on visual spray cone angle.

The discrepancy in observed spray cone angle between this investigation and the relations developed in previous research shown in Figure 18 may indicate the variability of optical measurement from random flow conditions. The probabilistic formation of droplets, for instance, especially in configurations with less atomization, may present some particles at a higher angle that do not comprise a significant fraction of the mass flow. As shown in Figure 14, the fine mist at the upper boundary of the spray cone can be more readily disregarded than droplets that may be ejected at a higher angle from sheet

breakup oscillations. Regardless, models for optical spray cone angle are shown in this data to converge with the observations of this experiment at higher momentum ratios. Because radial momentum is dominant at higher momentum ratios, this confirms  $\theta_v$  is primarily influenced by radial momentum rather than the direction of the mass flow.

The effect of uneven distribution of radial momentum on the spray cone is further demonstrated by the test at the highest  $TMR$  with each pintle. All of these tests showed two distinct peaks over the six intervals of  $\theta$  where mass was collected, visible as a smaller dot between two larger markers in a vertical run in Figure 12. This phenomenon, referred to as a double spray cone, emerges as the momentum ratio increases indicates that the presence of sufficient radial momentum allows some radial flow to separate from the remainder of the combined sheet. Although insufficient momentum ratios were tested to determine conclusively the momentum ratio at which this phenomenon emerges, the presence of the double spray cone on the highest  $TMR$  of each pintle tested suggests an inception in the range  $TMR \in (0.8, 1.1)$ .

## V. CONCLUSION AND FUTURE WORK

These results show that mass distribution in the spray cone from a pintle injector is not significantly affected by the use of multiple rows of staggered orifices up to  $H/D_o = 2.0$ . This can encourage the use of multiple rows of orifices for the desired benefits offered in injector design. However, when predicting flow patterns and heat transfer distribution for a spray cone, this investigation showed that at  $H/D_o \lesssim 1.0$  an optically-measured spray cone is greater than the angle at which most propellant mass propagates from the collision. Therefore, designs in this  $H/D_o \lesssim 1.0$  range, including pintle injectors with a single orifice row, should use mass flow distribution rather than optical spray cone to avoid pursuing a design that is overly reflective of the contribution of radial momentum.

The strong agreement between optical spray cone angle and the inverse-tangent of local momentum ratio supports the classical theory of an inelastic collision to describe pintle performance. Divergence between relations from previous work based on optical spray cone and the mass flow measurements presented here indicates that the upper spray cone surface is not representative of the actual mass flow distribution: rather, relations developed from optical spray cone exaggerate the effect of radial momentum on the direction of the combined spray at low momentum ratios.

Future work to expand on the results found here could reveal further details about these phenomena.

1. An upgraded mass flow distribution measurement apparatus could be created with welded or brazed connections between the dividers and slots in metal side plates. This would permit a greater resolution of the spray cone from smaller measurement intervals of  $\theta$ .
2. Labeling one of the propellant flows with a dye or solvent could investigate two other questions. First, evaluating the concentration of the label would assess mixing performance. Second, the mixing at different angular stations within the spray cone could assess hypotheses suggested by this work about the bypass flow by revealing which regions of the spray cone consist of a greater fraction of the axial propellant. This ability to sample mass through the spray cone is an additional capability of a mass flow distribution apparatus like that developed for this experiment compared to laser spray cone assessment methods, aside from the reduced hardware cost.
3. Additional tests could examine the  $TMR$  range where the double spray cone emerges and the minimum value of  $TMR$  at which  $\theta_v$  and  $\theta_m$  converge, indicating where the radial mass flow becomes dominant.
4. Direct study of the deflection  $\gamma$  of the bypass flow from a row of orifices would investigate the hypothesis posed by these results that the effect of orifice row spacing the apparent convergence of optical and mass flow spray cones near  $H/D_o \approx 1.0$  is driven by circumferential deflection of the axial flow by the first row of orifices.

The present work and the scope of future questions reflects the complexity of pintle injectors. Nonetheless, nondimensionalized investigation of key parameters, such as the  $H/D_o$  ratio, provide critical information to estimate behavior for design purposes. The results of this investigation emphasize the importance of considering the actual mass flow distribution realized in the spray cone, rather than the upper surface from optical measurements, to describe the impact of  $H/D_o$ .

## VI. ACKNOWLEDGEMENTS

This work would not have been possible without the collaboration and consultation of Kenrick Chan, Richard Burns, and Michael Mastrangelo of the Liquid Propulsion Lab at USC. Manufacturing of the pintle prototypes owes credit to Rodney Yates and Seth Weiman. Our faculty advisor, Dr. Robert Antypas, was essential in procuring the necessary materials and resources.

## VII. NOMENCLATURE

### Symbols

$D$	Diameter
$H$	Distance between rows of orifices
$L$	Axial distance between annulus and pintle orifices
$L_S$	Dimensionless skip distance between annulus and pintle orifices
$L_{SE}$	Effective skip distance to multiple rows of pintle orifices
$LMR$	Local momentum ratio
$\dot{m}$	Mass flow rate.
$TMR$	Total momentum ratio.
$r$	Radius

### Greek

$\rho$	Density
$\theta$	Spray cone angle
$\lambda$	Rate of change of spray cone angle with respect to total momentum ratio, $d\theta/d(TMR)$

### Subscripts

$a$	Axial
$m$	Mass-based
$p$	Pintle
$r$	Radial
$v$	Visual/optical-based

## VIII. REFERENCES

- [1] V. Yang, M. Habiballah, J. Hulka and M. Popp, *Liquid Rocket Thrust Chambers: Aspects of Modeling, Analysis, and Design*, Reston: American Institute of Aeronautics and Astronautics, 2004.
- [2] M. Son, K. Radhakrishnan, J. Koo, O. C. Kwon and H. D. Kim, "Design Procedure of a Movable Pintle Injector for Liquid Rocket Engines," *J. Propulsion and Power*, vol. 33, no. 4, pp. 858-869, 2017.
- [3] S. Lee, D. Kim, J. Yoo and Y. Yoon, "Spray characteristics of a pintle injector based on annular orifice area," *Acta Astronautica*, vol. 167, pp. 201-211, 2020.
- [4] G. Dressler and J. Bauer, "TRW Pintle Engine Heritage and Performance Characteristics," American Institute of Aeronautics and Astronautics, Redondo Beach, 2000.
- [5] W. Carter and G. Bell, "Development and Demonstration of a N2O4/N2H4 Injector," Air Force Rocket Propulsion Laboratory, Redondo Beach, 1969.
- [6] W. Hammock, E. Currie and C. Fisher, "Apollo Experience Report - Descent Propulsion System," National Aeronautics and Space Administration, Houston, 1973.
- [7] T. Mueller, "Pintle Injector Tip with Active Cooling". United States Patent 7,503,511, 17 March 2009.
- [8] R. Rezende, A. Pimenta and V. d. C. Perez, "Experiments with Pintle Injector Design and Development," in *Propulsion and Energy Forum*, Orlando, 2015.
- [9] "Boomie Zoomie: Overview," Purdue Students for the Exploration and Development of Space Team, 2021. [Online]. Available: <https://purdueseds.space/liquids/boomie-zoomie/>. [Accessed 4 December 2021].

- [10] J. Blakely, J. Freeberg and J. Hogge, "Spray Cone Formation from Pintle-Type Injector Systems in Liquid Rocket Engines," University of Southern California, Los Angeles, 2017.
- [11] D. W. Escher, "Design and Preliminary Hot Fire and Cold Flow Testing of Pintle Injectors," Pennsylvania State University, 1996.
- [12] M. Son, K. Yu, J. Koo, O. C. Kwon and J. S. Kim, "Effects of Momentum Ratio and Weber Number on Spray Half Angles of Liquid Controlled Pintle INjector," *J. Thermal Science*, vol. 24, no. 1, pp. 37-43, 2015.
- [13] J. Holdeman, "Mixing of Multiple Jets with a Confined Subsonic Crossflow," *Prog. Energy Combust. Sci.*, vol. 19, pp. 31-70, 1993.
- [14] S. Huang, Y. Li, J. Zhou, S. Liu and H. Peng, "Effects of the pintle injector on H<sub>2</sub>/air continuous rotating detonation wave in a hollow chamber," *International Journal of Hydrogen Energy*, vol. 44, no. 26, pp. 14044-14054, 2019.
- [15] G. Sutton and O. Biblarz, *Rocket Propulsion Elements*, 9th ed., Hoboken: Wiley, 2017.
- [16] B. Austin, S. Heister and W. Anderson, "Characterization of Pintle Engine Performance for Nontoxic Hypergolic Bipropellants," *J. Propulsion and Power*, vol. 21, no. 4, pp. 627-635, 2005.
- [17] X.-x. Fang and C.-b. Shen, "Study on atomization and combustion characteristics of LOX/methane pintle injectors," *Acta Astronautica*, vol. 136, pp. 369-379, 2017.
- [18] P. Cheng, Q. Li and H. Chen, "Flow characteristics of a pintle injector element," *Acta Astronautica*, vol. 154, pp. 61-66, 2019.
- [19] J. Blakely, J. Freeberg and J. Hogge, "Spray Cone Formation from Pintle-Type Injector Systems in Liquid Rocket Engines," in *AIAA Scitech Forum*, San Diego, 2019.
- [20] T. Ohrn, D. Senser and A. Lefebvre, "Geometrical Effects on Discharge Coefficients for Plain-Orifice Atomizers," *Atomization and Sprays*, vol. 1, no. 2, pp. 137-153, 1991.
- [21] D. Huzel and D. Huang, *Design of Liquid Propellant Rocket Engines*, Washington, D.C.: National Aeronautics and Space Administration, 1967.
- [22] W. Nurick, "Orifice Cavitation and Its Effect on Spray Mixing," *J. Fluids Eng.*, vol. 98, no. 4, pp. 681-687, 1976.
- [23] E. Lemmon, M. McLinden and D. Friend, "Thermophysical Properties of Fluid Systems," in *NIST Chemistry WebBook, NIST Standard Reference Database Number 69*, National Institute of Standards and Technology, 2021.
- [24] Y. Cengel and A. Ghajar, *Heat and Mass Transfer*, 5th ed., New York: McGraw Hill Education, 2015.
- [25] P. Wu, L. Tseng and G. Faeth, "Primary Breakup in Gas/Liquid Mixing Layers for Turbulent Liquids," *Atomization and Sprays*, vol. 2, pp. 295-317, 1992.
- [26] S. Lambiris and L. Combs, "Steady-state Combustion Measurements in a LOX/RP-1 Rocket Chamber and Related Spray Burning Analysis," in *Detonation and Two-Phase Flow*, New York, Academic Press Inc., 1962, pp. 269-304.
- [27] W. Penttermann and W. Wagner, "New pressure-density-temperature measurements and new rational equations for the saturated liquid and vapour densities of oxygen," *J. Chem. Thermodynamics*, vol. 10, no. 12, pp. 1161-1172, 1978.
- [28] B. McBride and S. Gordon, "Computer Program for Calculation of Complex Chemical Equilibrium Compositions and Applications," National Aeronautics and Space Administration, Cleveland, 1996.
- [29] S. Alexandi, N. Ang and K. Chan, *Water Flow Test Stand Test Procedures Document*, 2021.

## IX. APPENDICES

### A. DISCHARGE COEFFICIENT MEASUREMENT

To prepare to use the LPL WFTS for combined flow tests, the discharge coefficients of the annulus and pintle needed to be measured separately. This allowed the calculation of mass flow of each stream from the pressure registered in the sense lines attached upstream of the test article with a rearrangement of (2).

Pressure transducer and load cell data from the LPL WFTS were processed using MATLAB. Noise in mass flow data was smoothed using a Fast Fourier Transform algorithm to eliminate high frequency, low amplitude components of the signal. Cleaned data was used to facilitate the selection of the steady-state region of the test. A linear regression was performed over this time range to determine the mass flow rate. Uncertainty was determined by the maximum and minimum slope that remained bounded within the 95% confidence interval of the best-fit line.

As Figure 19 illustrates, a slight startup transient is notable in approximately the first two seconds of water flow. Rather than the rate at which mass enters the load cell increasing, which would be represented in a concave-up curve, the slope of the plot decreases to the steady-state slope. This arises from the inertia of the water striking the load cells, represented at the end of a flow test by a rapid drop in registered force. This force, however, is constant during the steady-state flow and therefore does not affect the slope of the best-fit line used to calculate mass flow.

Consistent data were returned for flow through the pintle and annulus, providing discharge coefficients for use in determining mass flow rate based on element pressure drop during combined-flow tests, as shown in Table 10 and Figure 20. As Figure 20 shows, and observed by Ohrn et al., discharge coefficient is constant with Reynolds number, which is directly proportional to mass flow rate and velocity [20]. Therefore, the tests validated discharge coefficients over the momentum ranges considered for this study and give the calibration data needed to perform tests over the desired range of  $TMR$ .

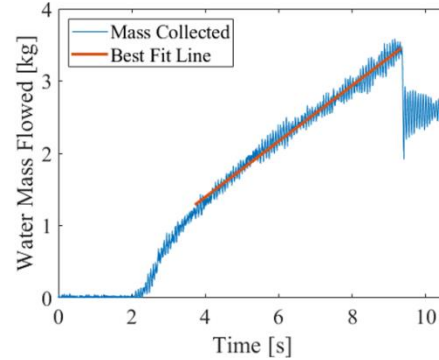


Figure 19. Sample of MATLAB data processing for mass flow rate, showing raw data collection and the best fit line used to calculate mass flow rate.

Table 10. Discharge coefficient results from single flow tests.

	<b>Pintle</b>		<b>Annulus</b>	
$C_d$	0.60		0.57	
$\sigma$	2.8%		2.3%	
$N$	11		9	
$\Delta C_d$	4%		3%	
	<b>Min</b>	<b>Max</b>	<b>Min</b>	<b>Max</b>
$\dot{m}$ [kg/s]	0.50	1.16	0.29	0.52
$\Delta P$ [kPa]	50	1144	334	1159
	<b>Minimum</b>		<b>Maximum</b>	
$TMR$	0.45		7.71	

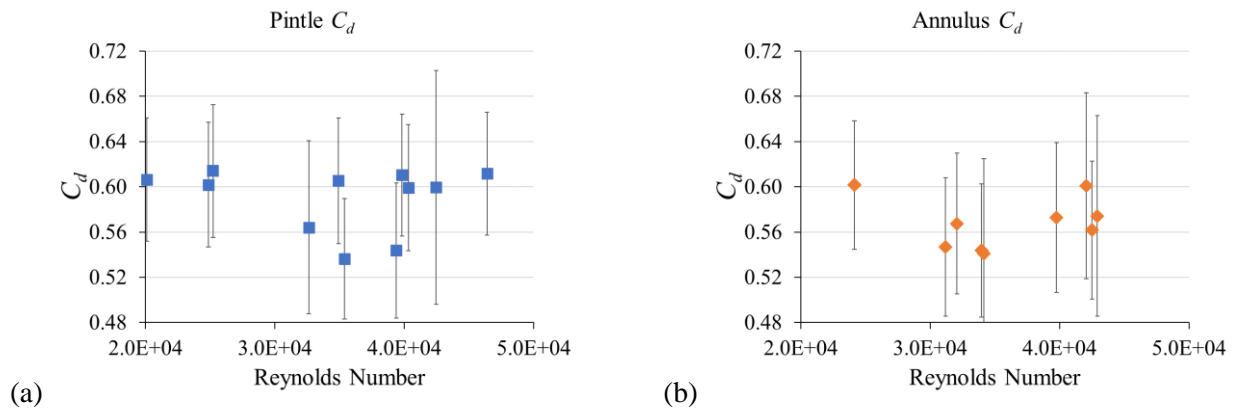


Figure 20. Discharge coefficients measured for (a) the pintle and (b) annulus in single flow testing.



## B. UNCERTAINTY CALCULATION

### 1. Discharge Coefficient

The uncertainty for a single measurement of  $C_d$  was obtained from uncertainty propagation for the measured quantities in (2) as

$$\frac{\Delta C_d}{C_d} = \sqrt{\left(\frac{\Delta \dot{m}}{\dot{m}}\right)^2 + \left(\frac{\Delta A}{A}\right)^2 + \left(\frac{\Delta \rho}{2\rho}\right)^2 + \left(\frac{\Delta(\Delta P)}{2\Delta P}\right)^2} \quad (10)$$

Since  $\dot{m}$  is measured from the slope of the best fit line,  $\Delta \dot{m}$  is determined from the standard error  $\delta$  of the best fit line produced by the MATLAB functions `polyfit` and `polyval`. The upper bound of  $\dot{m}$  is the slope of the line from  $(m - \delta)|_{t=t_0}$  at the start time to  $(m + \delta)|_{t=t_f}$  at the end of the test. Analogously, the lower bound of  $\dot{m}$  is the slope of the line from  $(m + \delta)|_{t=t_0}$  to  $(m - \delta)|_{t=t_f}$ .

$\Delta \rho$  is negligible compared to the other uncertainty quantities.

$\Delta A$  was determined from measurement of the aluminum injector prototype. Measurements at the USC Baum Family MakerSpace for the pintle outer diameter and the outer diameter of the hole for the annulus in the lower manifold are given in Table 11.

For the annulus, uncertainty propagation yields an uncertainty as

$$\frac{\Delta A_{ann}}{A} = \sqrt{\left(\frac{2\Delta r_{out}r_{out}}{r_{out}^2 - r_{in}^2}\right)^2 + \left(\frac{2\Delta r_{in}r_{in}}{r_{out}^2 - r_{in}^2}\right)^2} \quad (11)$$

The radial holes in the pintle are reamed, with a precision of 0.001in, giving an uncertainty from

$$\frac{\Delta A}{A} = \frac{2\Delta r}{r} \quad (12)$$

$\Delta P$  was determined from the pressure fluctuations as

$$\Delta P = \frac{P_{max} - P_{min}}{2} \quad (13)$$

For the uncertainty of the average value of  $C_d$  used for calculation of downstream parameters, the t-estimator method was used to reflect the low variation of  $C_d$  across the samples measured. While this uncertainty is lower than that of an individual measurement of  $C_d$ , it reflects the repetition of the measurement value over a large number of samples.

### 2. Optical Spray Cone Angle

To determine uncertainty for optical spray cone measurements, (14), (15), (16), and (17) were used in reference to measurements defined by Figure 21. There are two separate points of uncertainty in the optical measurement of spray cone angle.

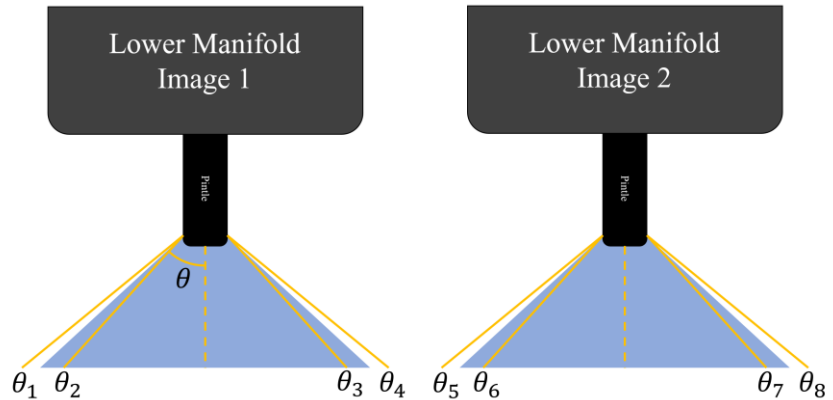


Figure 21. Spray cone angle optical analysis uncertainty reference.

Table 11. Measurements of pintle outer diameter used for calculation of injection area uncertainty. All measurements are  $\pm 0.0001$  in. The pintle for  $H/D_o$  was manufactured in the AME 441 lab, while the remainder were machined by the Viterbi/Dornsife Machine Shop.

$H/D_o$	$D_p$ [in]	Annulus OD [in]
0.0	0.7415	0.7660
0.5	0.7410	
1.0	0.7429	
1.5	0.7429	
2.0	0.7416	
Nominal	0.7420	0.7670

The first contribution to uncertainty in measuring any given edge of the spray is shown in (14, where  $\Delta\theta_{edge}$  is defined as one half the difference between the upper and lower boundary for a guess of where the edge of the spray lies.

$$\Delta\theta_{edge} = \frac{1}{2} \max(\theta_1 - \theta_2; \theta_4 - \theta_3; \theta_5 - \theta_6; \theta_8 - \theta_7) \quad (14)$$

The second uncertainty in the measurement is shown in (15, where  $\Delta\theta_{symmetry}$  is defined as one half the difference between the left and right-side measurements of one sample image.

$$\Delta\theta_{symmetry} = \frac{1}{2} \max\left(\frac{\theta_1 + \theta_2}{2} - \frac{\theta_3 + \theta_4}{2}; \frac{\theta_5 + \theta_6}{2} - \frac{\theta_7 + \theta_8}{2}\right) \quad (15)$$

The spray cone angle is derived from the average of all eight measurements taken from a single TMR and  $H/D_o$  configuration as shown in Equation (16).

$$\theta_{avg} = \frac{\theta_1 + \theta_2 + \theta_3 + \theta_4 + \theta_5 + \theta_6 + \theta_7 + \theta_8}{8} \quad (16)$$

Overall, the maximum value of both  $\Delta\theta_{edge}$  and  $\Delta\theta_{symmetry}$  are added to find the total uncertainty of the measurement. Total uncertainty is then added to  $\theta_{avg}$  to find the final spray cone angle as seen in Equation (17.

$$\theta_{spray\ cone} = \theta_{avg} \pm (\Delta\theta_{edge} + \Delta\theta_{symmetry}) \quad (17)$$

### 3. Mass Flow Spray Cone Angle

The 5° interval of  $\theta$  used in the mass flow distribution measurement apparatus means that the measurement of an angle for a stream of mass flow in the spray cone could vary within  $\pm 2.5^\circ$  of the reported value. Fluctuations in mass flow during the test from supply pressure variation and startup and shutdown transients would be represented in a difference between the peak spray cone angle and the centroid spray angle. As a result of these two contributions, the uncertainty in  $\theta_m$  was calculated as

$$\Delta\theta_m = |\theta_{centroid} - \theta_{peak}| + 2.5^\circ \quad (18)$$

### 4. Total Momentum Ratio

For TMR,  $\dot{m}$  is a calculated quantity from the pressure recorded at the transducer upstream of the injector. The uncertainty in calculated mass flow from (2) is

$$\frac{\Delta\dot{m}}{\dot{m}} = \sqrt{\left(\frac{\Delta C_d}{C_d}\right)^2 + \left(\frac{\Delta A}{A}\right)^2 + \left(\frac{\Delta\rho}{2\rho}\right)^2 + \left(\frac{\Delta(\Delta P)}{2\Delta P}\right)^2} \quad (19)$$

Uncertainty propagation from (4), substituting for  $\Delta\dot{m}/\dot{m}$  using (19) yields

$$\frac{\Delta TMR}{TMR} = \sqrt{\left(4\left(\left(\frac{\Delta C_d}{C_d}\right)^2 + \left(\frac{\Delta A}{A}\right)^2 + \left(\frac{\Delta\rho}{2\rho}\right)^2 + \left(\frac{\Delta(\Delta P)}{2\Delta P}\right)^2\right) + \left(\frac{\Delta\rho_a}{\rho_a}\right)^2 + \left(\frac{\Delta A_a}{A_a}\right)^2\right)_{annulus} + \left(4\left(\left(\frac{\Delta C_d}{C_d}\right)^2 + \left(\frac{\Delta A}{A}\right)^2 + \left(\frac{\Delta\rho}{2\rho}\right)^2 + \left(\frac{\Delta(\Delta P)}{2\Delta P}\right)^2\right) + \left(\frac{\Delta\rho_a}{\rho_a}\right)^2 + \left(\frac{\Delta A_a}{A_a}\right)^2\right)_{pintle}} \quad (20)$$

## C. TEST ARTICLE DESIGN AND DEVELOPMENT

The injector used in this investigation was sized for an engine intended for a small, student-built flight vehicle. As a result, a limited range of composite materials and metals were available, with the use only of manual machines an additional constraint on possible geometries. Thrust and firing time were estimated from performance goals for the vehicle. Chamber pressure was maximized for from the thickness of the combustion chamber wall possible in a layup, minus expected ablation [21] and with a factor of safety of 2. The pressure drop across the injector elements was selected to provide at least 25% of chamber pressure to prevent intrusion of combustion products into the injector, while the upper bound was determined by the

capabilities of an upstream piping system in development for a hot firing.

Using these parameters, a NASA CEA analysis was used to optimize mixture ratio by meeting the required parameters with minimal mass flow rate. These results and the chamber fluid properties used to dimension the nozzle and inform heat transfer analyses, are presented in Table 13.

To appropriately specify geometric parameters for the measurement apparatus and the injector using Equations (2) and (3), the discharge coefficient and expected droplet diameter produced by the pintle orifices needed to be calculated. The discharge coefficient calculation followed the algorithm developed by Nurick et al. to check for cavitation, using the properties for liquid oxygen and water given in Table 14 [22].

The values calculated for liquid oxygen were used for the design of the injector, while the discharge coefficient of the injector for water was used to inform the pressure drop calculations presented in Section III. Using guesses at orifice diameter from initial runs, liquid oxygen droplet diameter calculated using the empirical relationship presented by Wu [25] to represent a droplet with the same surface-to-area ratio as the overall flow:

$$D_{32} = 133.0 \left( \frac{D_o}{8} \right) We^{-0.74} \quad (21)$$

where  $We$  is the Weber number, a dimensionless number used to describe the ratio of fluid inertia to fluid cohesion:

$$We = \frac{\rho v^2 L}{\sigma} \quad (22)$$

From these formulas, the orifice diameter was iteratively confirmed as the final geometry was selected. Charts from [26] allowed estimation of combustion time for a droplet of this size as 0.001s.

With projected combustion behavior, (2) was used with classical momentum calculations to approximately place the flame from the spray cone based on a set of manufacturing inputs. The fluid parameters in Table 13 and Table 14 iteratively based on a selected combustion region. The geometry selection in Table 3 led to the outputs in Table 15. Although only one combination is shown, the program iterated through thousands of possibilities to optimize the result.

Table 15. Outputs of simplified injector sizing function for a single set of input parameters. The program iterated through many parameter combinations, but the values shown here are for the selected geometry combination presented in Table 3.

Output	Oxidizer (Pintle)	Fuel (Annulus)
$v_s$ [m/s]	30.03	38.71
$\Delta P$ [MPa]	0.739	0.757
Estimated Combustion Distance from Pintle [mm]	54	

Table 12. High-level design requirements for the engine design used as a test subject in this experiment.

Fuel	RP-1/Jet-A
Fuel Temperature	300 K
Oxidizer	Liquid Oxygen
Oxidizer Temperature	100 K
Thrust	1200 lbf
Firing Time	15 s
Chamber Pressure	400 psi
Nozzle Exit Pressure	57.2 kPa
Target Injector $\Delta P$	$100 \text{ psi} \leq \Delta P \leq 150 \text{ psi}$

Table 13. Chamber parameters for the engine design used as a test subject in this experiment based on the design requirements in Table 12 and CEA analysis.

Chamber Temperature	3517 K
Fuel Mass Flow Rate	0.653 kg/s
Oxidizer Mass Flow Rate	1.415 kg/s
Oxidizer/Fuel Ratio	2.2
Chamber Temperature	3517 K
Specific Gas Constant	378.1 J/kg/K
Specific Heat Ratio	1.164

Table 14. Inputs and outputs of discharge coefficient calculation. Except where indicated, sources are [23] for liquid oxygen and [24] for liquid water.

Property	Design: Liquid Oxygen, 100K	Test: Water, 300 K
$\rho$ [kg/m <sup>3</sup> ]	1088	998
$\mu$ [kg/m/s]	$1.526 \times 10^{-4}$	$1.002 \times 10^{-3}$
$P_{vap}$ [Pa]	253180	2339
$\sigma$ [N/m]	0.0108	0.0717
$C_d$	0.815 [22]	0.857 [22]
$v$ [m/s]	30.03 (calculated from (2) and (3))	31.36 (calculated from (2) and (3))

# D. WFTS PIPING AND INSTRUMENTATION DIAGRAM (P&ID)

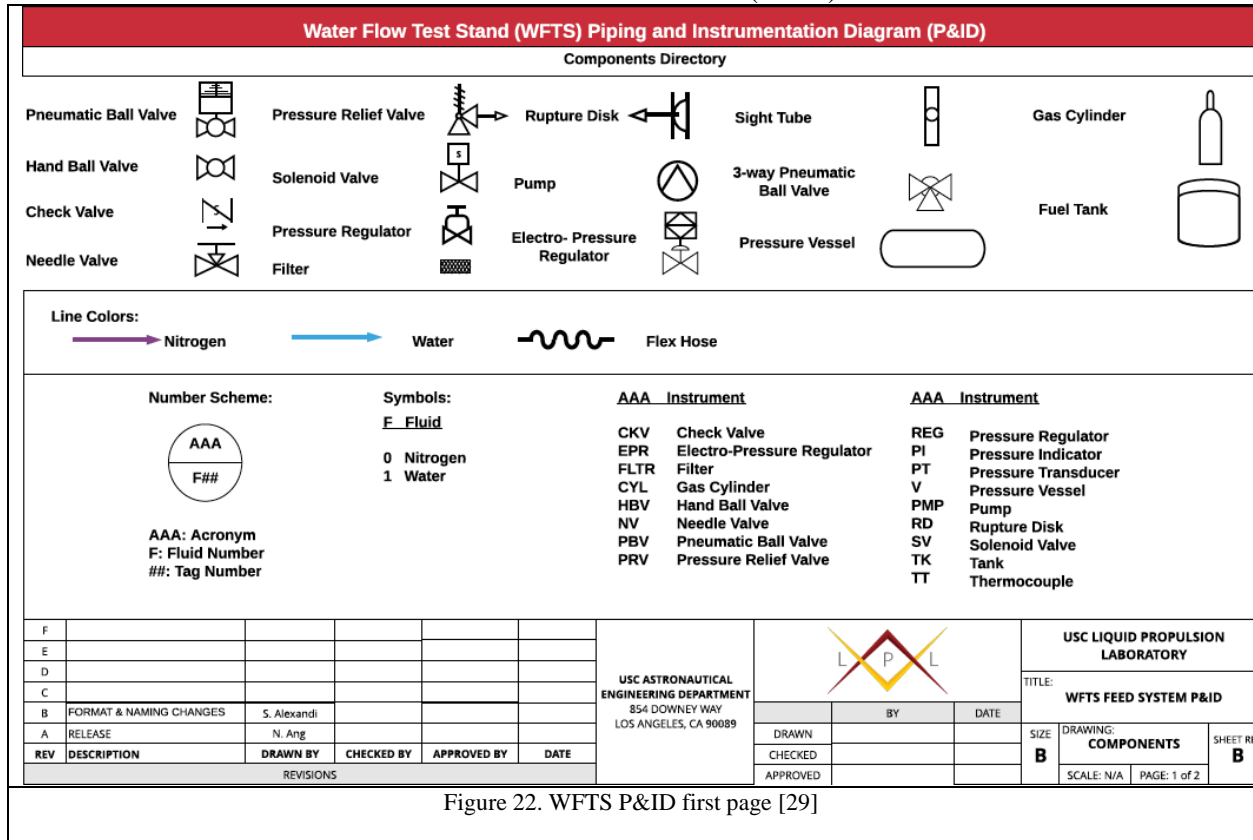


Figure 22. WFTS P&ID first page [29]

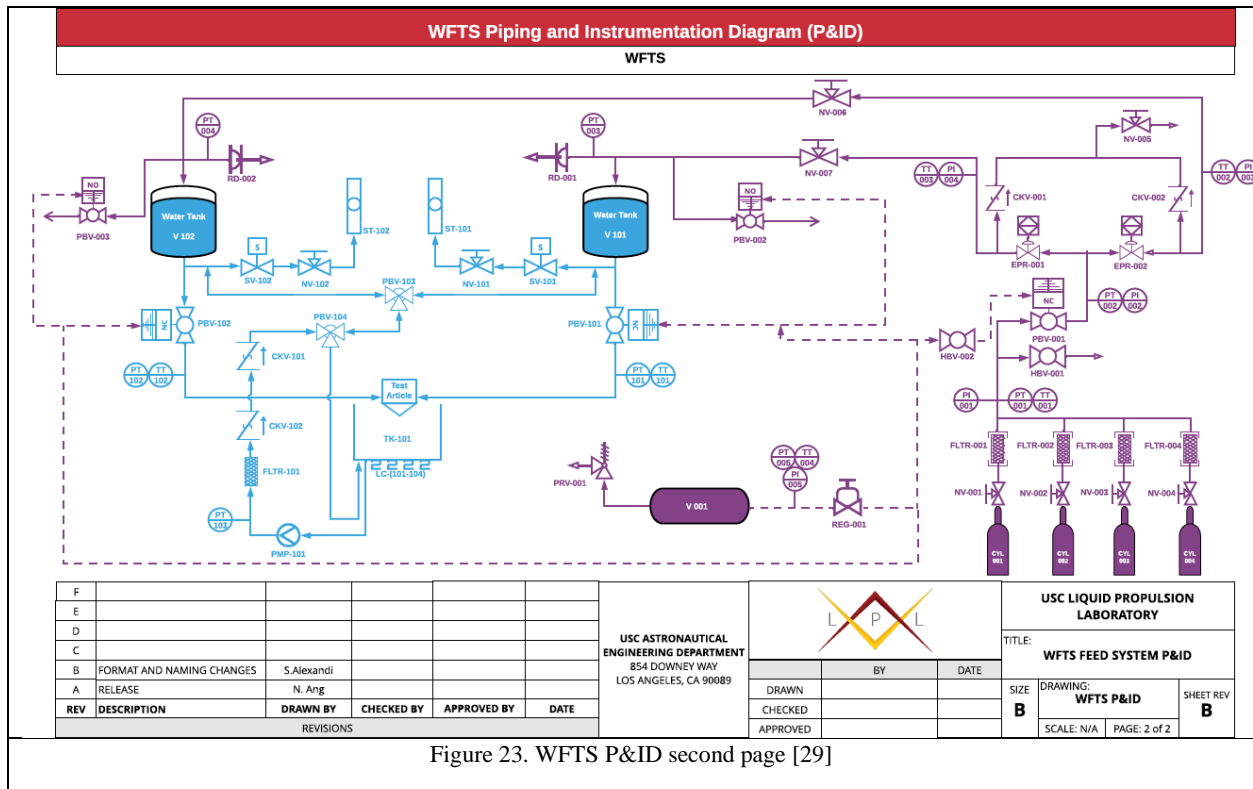


Figure 23. WFTS P&ID second page [29]

## E. IMPORTANT SENSORS TABLE

Table 16. WFTS key sensors specifications					
Sensor ID	Model	Range	Output	Accuracy	Location
LC1-W4	Omega LCCA-50	50 lbf	3 mV/V	±0.037% FS	Water collection basin
LC2-W4	Omega LCCA-50	50 lbf	3 mV/V	±0.037% FS	Water collection basin
LC3-W4	Omega LCCA-50	50 lbf	3 mV/V	±0.037% FS	Water collection basin
LC4-W4	Omega LCCA-50	50 lbf	3 mV/V	±0.037% FS	Water collection basin
PT-W1	PX319-1KG5V	1000 psig	0-5 Vdc	±0.25% BSL	Test article – Fuel
PT-W2	PX319-1KG5V	1000 psig	0-5 Vdc	±0.25% BSL	Test article – Oxidizer
PT-P1	PX319-1KG5V	1000 psig	0-5 Vdc	±0.25% BSL	Tank 1
PT-P2	PX319-1KG5V	1000 psig	0-5 Vdc	±0.25% BSL	Tank 2

## F. TEST MATRIX INPUTS

To further illustrate the parameters of each test run, a sample of a pintle test table is provided below. The table describes the tank set pressures needed to overcome feed system pressure drop to achieve the desired injection pressure drop for the appropriate *TMR*. The angle ranges describing the interval of  $\theta$  for which a vinyl flow diverter was assigned to a bin are specified. Initial test runs not used for the numerical data presented in this report were used to determine the appropriate bin angle range. Experience over multiple runs also allowed determination of the tank set pressure required to account for the aforementioned electronic pressure regulator behavior and the feed system pressure drop required to achieve the desired injector element pressure drop.

Table 17. Sample test operation matrix.						
<i>TMR</i>		0.35	0.47	0.6	0.8	1.1
Pintle Pressure Drop		20	27	34	45	62
Pintle Tank Flow Pressure		23	32	41	53	71
Pintle Tank Set Pressure		23	32	41	53	71
Annulus Pressure Drop		130	130	130	130	130
Annulus Tank Flow Pressure		138	138	138	138	138
Annulus Tank Set Pressure		141	141	141	141	141
Expected Spray Cone Angle		22.5	27.5	37.5	42.5	47.5
Bin Ranges	6	10-15	20-25	25-30	30-35	40-45
	5	15-20	25-30	30-35	35-40	45-50
	4	20-25	30-35	35-40	40-45	50-55
	3	25-30	35-40	40-45	45-50	55-60
	2	30-35	40-45	45-50	50-55	60-65
	1	35-40	45-50	50-55	55-60	65-70